Article:
Sekar, Karthikeyan, Kassam, Ahmed, Bai, Yang et al. (2021) Hierarchical bismuth vanadate/reduced graphene oxide composite photocatalyst for hydrogen evolution and bisphenol A degradation. Applied Material Today. 100963. ISSN: 2352-9407

https://doi.org/10.1016/j.apmt.2021.100963

Hierarchical bismuth vanadate/reduced graphene oxide composite photocatalyst for hydrogen evolution and bisphenol A degradation

Sekar Karthikeyan,[a,b,e*] Ahmed Kassam,[a] Yang Bai,[a] Ben Coulson,[c] Wei Li,[a*] Richard E. Douthwaite,[c] Keiko Sasaki,[b*] Adam F. Lee,[d*]

[a]Aston Institute of Materials Research, European Bioenergy Research Institute, Aston University, Birmingham B4 7ET, UK

[b]Department of Earth Resources Engineering, Faculty of Engineering, Kyushu University, Fukuoka 819-0395, Japan

[c]Department of Chemistry, University of York, York YO10 5DD, UK

[d]Centre for Advanced Materials & Industrial Chemistry (CAMIC), School of Science, RMIT University, Melbourne VIC 3000, Australia.

[e] Department of Chemistry and Biotechnology, School of Engineering, The University of Tokyo, 7-3-1 Hongo, Bunkyo-ku, Tokyo 113-8656, Japan

* Corresponding authors: Tel: +0121 204 3035; +61 399252623, E-mail: karthik.keyan02@gmail.com w.li8@aston.ac.uk; keikos@mine.kyushu-u.ac; adam.lee2@rmit.edu.au

Abstract:

Bismuth vanadate ($BiVO_4$) is a widely studied photocatalyst for the depollution of contaminated wastewater, production of hydrogen by water splitting, and organic synthesis. The photophysical properties of $BiVO_4$ are sensitive to morphology and quantum confinement effects, and can exhibit enhanced photocatalytic performance in nanocomposites with graphene. Synthesis of hierarchical $BiVO_4$ plates decorated by nanoparticles (h-$BiVO_4$) in contact with reduced graphene oxide (RGO) is reported via a facile one-pot solution phase approach using ethanolamine and a polyethylene glycol stabilizer. The resulting h-$BiVO_4$/RGO photocatalyst exhibited superior photoactivity for bisphenol A (BPA) degradation and hydrogen evolution under visible light irradiation compared to single component h-$BiVO_4$ or a μm-sized block-like $BiVO_4$ morphology. Rates of BPA photocatalytic degradation and apparent quantum efficiency (AQE) decreased in the order h-$BiVO_4$/RGO (4.5×10^{-2} mmol.g^{-1}.min^{-1}; 15.1 % AQE) > h-$BiVO_4$ (3.5×10^{-2} mmol.g^{-1}.min^{-1}; 11.7 % AQE) > $BiVO_4$ (1×10^{-2} mmol.g^{-1}.min^{-1}; 3.4 % AQE), representing a 4.5 fold enhancement for h-$BiVO_4$/RGO versus $BiVO_4$. Liquid phase photodegradation products included benzene-1,4-diol, cyclohexa-2,5-diene-1,4-dione and (2Z)-but-2-enedioic acid. The rate of photocatalytic hydrogen production under visible light was 11.5 μmol.g^{-1}.h^{-1} for h-$BiVO_4$/RGO, ~383.3 times greater than for $BiVO_4$ (0.03μmol.g^{-1}.h^{-1}). The superior photocatalytic performance of h-$BiVO_4$/RGO is largely attributed to its higher surface area, aided by enhanced visible light absorption and charge separation across the semiconductor-RGO interface, which together confer a higher density and lifetime of photoexcited charge carriers.

Keywords: $BiVO_4$, nanoparticles, reduced graphene oxide, photocatalyst, bisphenol A, hydrogen.

Introduction

Clean energy is recognised as a key challenge in the 2030 United Nations Sustainable Development Goals, with climate change and increasing regional concerns over energy security driving the transition to low carbon energy resources that minimize environmental impact. Solar energy is an abundant renewable energy source for power generation, water splitting and environmental remediation that could help meet some of these challenges.[1, 2] However, low sunlight-to-chemical energy conversion efficiencies and/or a reliance on noble metals necessitates the development of next-generation materials incorporating Earth abundant elements and offering significant photocatalytic activity.[1] Many classes of inorganic semiconductor (e.g. TiO_2, ZnO, Fe_2O_3, Cu_2O, CdS), composite (e.g. CdS/graphene, Bi_2MoO_6–BiOCl, graphene-TiO_2), noble metal (Ag, Au, Pt, Pd) and hybrid (e.g. organic–inorganic, carbon quantum dot/Bi_2WO_6, CdSe-Au) nanomaterials have been studied as photocatalysts for energy production and environmental remediation.[3-9] Unfortunately, such catalysts typically require complex syntheses and expensive co-catalysts to enhance visible light (~43 % of the solar spectrum) photoactivity, in addition to limited stability.

Bismuth vanadate ($BiVO_4$) is an n-type semiconductor with a 2.4 eV bandgap, and is considered an environmentally benign photocatalyst for O_2 evolution and environmental remediation under visible irradiation ($\lambda > 420$ nm).[10] However, to our knowledge H_2 evolution from water splitting has not been reported using $BiVO_4$ photocatalysts under visible light, presumably due to the mismatch between the conduction band (CB) potential (ca. + 0.46 V vs NHE at pH = 0) and the reduction potential of water (0 V vs NHE).[11] Quantum dot (QD) metal oxide and sulphide (e.g. Bi_2O_3, $BiVO_4$, CuO–In_2O_3, CdS, CdTe, MoS_2) photocatalysts have received significant attention as visible light photocatalysts for water splitting and the decomposition of organic pollutants.[12-15] Sun et al. reported that $BiVO_4$ nanoparticle photocatalysts had a CB more negative than the H^+/H_2 redox potential and were hence able to split water (0.22 $\mu mol_{H2}.h^{-1}$) under sunlight.[16] Carbon dot and $BiVO_4$ quantum dot composites featuring a high optical absorption coefficient and high stability, exhibit favourable visible light energy conversion increasing photocatalytic activity (0.92 $\mu mol_{H2}.h^{-1}$) at an apparent quantum efficiency (AQE) of 0.6 %.[17] Such QD-$BiVO_4$ photocatalysts presumably benefit from quantum coherence and confinement effects which modulate their electronic band structure and surface termination, potentially offering enhanced photochemical stability, faster charge carrier transport, higher quantum yields, and supressed charge carrier recombination. Wang et al. recently reported that the nanoscale dimensions of QD-$BiVO_4$ could greatly reduce the distance for photogenerated charge carriers to reach adsorbates to drive visible light photocatalysis.[18] Technological challenges remain for the scale-up and recovery of powder photocatalysts in industrial applications, and hence simple catalyst syntheses that avoid costly reagents, and high stability and easy separation in-use, are sought to limit waste by-products and increase lifetime, and hence improve economic feasibility and environmental protection.

Graphene has attracted significant attention since its discovery in 2004,[19] due to the two dimensional (2D) lamellar structure and high specific surface area (>2,600 $m^2\ g^{-1}$)[20], and excellent optical, electronic conductivity and mechanical properties.[21] Graphene is a zero bandgap semiconductor with a symmetrical band

structure, and can function as either a p- or n-type semiconductor through tuning of its structural and electronic properties.[22] The combination of metal oxide photocatalysts such as TiO_2, ZnO, Fe_2O_3, Cu_2O and $BiVO_4$ with graphene in p or p-n junction configurations can enhance visible light absorption, and extend electron-hole pair lifetimes and charge transport properties which can result in high activity nanocomposite photocatalysts.[23, 24] Other low dimensional nanomaterials e.g. graphitic carbon nitride, share similar properties to graphene (high surface area and high electronic conductivity) and have also been explored as composite photocatalysts, including with vanadates.[25] Graphene may act as a co-catalyst, photosensitizer, electron trap and charge transfer mediator, but is susceptible to aggregation of graphene sheets due to strong van der Waals forces.[26] Deeper insight into charge transport across semiconductor/graphene interfaces is also necessary to better understand the resulting modification of photocatalytic activity and selectivity.

Bisphenol A (BPA) is a known endocrine disrupting chemical (EDC), and commonly used as a raw material for production of epoxy resins and polycarbonate plastics,[27] such as water bottles, tableware and food packing materials. Reports have indicated that the demand for BPA was ca. 5 million tons in 2010, which has significantly increased year on year in recent times. This means that the regular usage of BPA contributes to the release of large amounts of persistent organic compounds into wastewater.[28] Reports indicate that BPA is toxic to wildlife and has significant adverse effects on human health, such as estrogenic activity, breast cancer, liver damage, cardiovascular disease and thyroid hormone disruption. BPA is classified as an EDC by the U.S. Environmental Protection Agency,[29] and hence simple and energy efficient technologies for its removal from aquatic systems are highly desirable.[30, 31]

Herein, the synthesis of $BiVO_4$ hierarchical nanostructures (h-$BiVO_4$) comprising plates decorated with nanoparticles, and their integration with 2D reduced graphene oxide (RGO) by a simple hydrothermal process, is described. The h-$BiVO_4$/RGO photocatalyst is active for the degradation of BPA to monocyclic quinones and maleic acid, and the production of H_2 from water, under visible light irradiation. Quantum confinement effects and a strong interfacial interaction within a h-$BiVO_4$/RGO nanocomposite suppress recombination and increase the density of photogenerated electron-hole charge carriers, possibly by charge separation across the interface, enhancing visible light response and photocatalytic performance.

Experimental

Chemicals

Bismuth (III) nitrate (Bi $(NO_3)_3 \cdot 5H_2O$, Aldrich, 99%), ammonium metavanadate (Alfa Aesar, NH_4VO_3 99.0%), nitric acid (Fisher Chemical, HNO_3 70%), ethanolamine (Aldrich, 98%), polyethylene glycol (Alfa Aesar), bisphenol A (Aldrich, ≥ 99%), H_2O HPLC grade (Sigma), acetonitrile (Sigma, 99.93% HPLC grade) and sodium sulphate (Sigma, 99%) were used as received.

Synthesis of h-$BiVO_4$/RGO

The GO synthesis procedure was as described in a previous report.[32] A h-$BiVO_4$/RGO nanocomposite was prepared by ultrasonication of 10 mg of GO in 100 mL deionized water for 2 h. In parallel, 50 mL of 0.1 M aqueous bismuth (III) nitrate was dispersed in 20 mL of 0.2 M aqueous ammonium metavanadate and 0.5 mL of 0.06 M polyethylene glycol to give a yellow-red solution. This mixture was then transferred to the GO solution at 50 °C, followed by dropwise addition of 10 mL of 2 M HNO_3 resulting in a clear yellow solution, and stirred at 400 rpm for 25 min. 5 mL of 0.1 M aqueous ethanolamine was then added dropwise to the mixture and stirring continued at 50 °C for a further 10 min, resulting in a reddish yellow precipitate. The reaction solution was then transferred to a 200 mL sealed Teflon-lined autoclave and placed in an air oven at 160 °C for 24 h, and then cooled to room temperature. The solid precipitate was isolated by centrifugation (7 min at 10,000 rpm) and washed four times with H_2O, and then three times with ethanol, before in vacuo drying for 12 h at 65 °C. The h-$BiVO_4$/RGO solid product was stored in a vacuum desiccator for further characterization. Note that this nanocomposite only contained 2 wt% RGO, and hence corresponding photophysical properties do not represent a superposition of those from the vanadate and RGO components. A h-$BiVO_4$ was also synthesized as above in the absence of GO, and a pure $BiVO_4$ sample synthesis without GO or PEG and substituting 5 mL of 0.5 M ammonium hydroxide instead of ethanolamine.

Photoelectrochemical characterization

A homogenous colloidal solution was prepared by sonication of photocatalyst powder (5 mg) and Nafion (10 μL, 5 wt%) dispersed in a mixture of water/ethanol (1 mL, 3:1 v/v) for 30 min. 5 μL of the colloidal solution was then deposited on a glassy carbon electrode (3 mm diameter) as a working electrode in a three-electrode photoelectrochemical cell; Pt wire was used as the counter electrode, and Hg/Hg_2SO_4 served as the reference electrode. The electrolyte (0.5 M Na_2SO_4) was purged in N_2 for 30 min. The light source was a 200 W Hg-Xe arc lamp fitted with a cut-off filter (λ >420 nm). Electrochemical measurements were performed using an Autolab potentiostat with Nova software. The electrode potential (V vs. Hg/Hg_2SO_4) was converted to the normal hydrogen electrode (NHE) using **Eq. 1**;[33] the electrolyte pH was 6.8 and E_{Hg/Hg_2SO_4} = 0.64 V:

$$E_{FB(vs.\ NHE)} = E_{FB(vs.Hg/Hg_2SO_4)} + E_{Hg/Hg_2SO_4} + 0.059 \times pH \qquad \textbf{Eq. 1}$$

Photocatalytic oxidation of BPA

Photocatalytic oxidative degradation of BPA was performed in a sealed 260 mL quartz photoreactor at room temperature. 20 mg of synthesized catalyst with 50 mL of 4.2×10^{-2} mM aqueous BPA solution was ultrasonicated for 7 min followed by stirring for 120 min in the dark to equilibrate any BPA adsorption prior to irradiation. The above reaction solution was subsequently irradiated by a 200 W Hg-Xe arc lamp (Oriel Instruments 66002) fitted with a 420 nm cut-off filter to exclude UV radiation. The irradiance inside the reactor was 16.7 $mW.cm^{-2}$. A 1 mL aliquot of the reaction mixture was periodically collected for analysis using an

Agilent 1260 Infinity Quaternary HPLC equipped with UV diode array (270 nm detection wavelength) and refractive index detectors; an Agilent Zorbax Eclipse plus C18 column was employed at 35 °C, and 1 mL/min of a 15 vol% acetonitrile/85 vol% HPLC grade water as the mobile phase. Post-reaction, the h-$BiVO_4$/RGO catalyst was separated from the reaction mixture by 5 min centrifugation at 10,000 rpm and dried at 60 °C in a vacuum air oven prior to characterization. Concentrations of BPA and liquid phase by-products, primarily hydroquinone (HQ), benzoquinone (BQ) and maleic acid (MA) were determined by HPLC using calibration against standard solutions of these compounds. The degree of BPA removal and corresponding product selectivity were calculated using **Eqs. 2** and **3** respectively. Photocatalytic reactions were repeated three times to ensure reproducibility, with HPLC injection performed in triplicate.

$$\text{BPA removal (\%)} = \frac{[\text{BPA intial}]-[\text{BPA final}]}{[\text{BPA initial}]} \times 100 \qquad \textbf{Eq. 2}$$

$$\text{Yield (\%)} = \frac{\text{Product mmol}}{\text{BPA converted mmol}} \times 100 \qquad \textbf{Eq. 3}$$

Hydrogen evolution

Hydrogen evolution was investigated using a 384 mL sealed quartz photoreactor at room temperature under irradiation by a 200 W Hg-Xe arc lamp. Typically, 50 mg of photocatalyst was mixed with 50 mL of pure water containing 0.5 mL of ethanol (as a hole scavenger) under sonication for 5 min to ensure a uniform distribution of reactants. Prior to irradiation, the reactor was purged with He for 1 h to remove residual oxygen and degas the solution. Aliquots of the reaction mixture were periodically collected in a 1 mL gas syringe for analysis using a Shimadzu Tracera GC-2010 Plus GC system fitted with a Carboxen 1010 column (30 m × 0.53 mm × 0.1 μm) and a barrier ionization detector (He as carrier gas).

Results and discussion

The hydrothermally synthesized h-$BiVO_4$ and h-$BiVO_4$/RGO heterojunction nanocomposite were first examined by high resolution transmission electron microscopy (HR-TEM, **Figure 1, S1-2**) and field-emission scanning electron microscopy (FE-SEM, **Figure S3**). Corresponding images for bulk-like $BiVO_4$ are shown in **Figure S4**. The h-$BiVO_4$/RGO comprised graphene sheets decorated by $BiVO_4$ plates of approximately ~150 nm diameter (**Figure 1b**, inset) and a high degree of crystallinity from powder X-ray diffraction (XRD, **Figure 2a**). The interplanar lattice spacing within these plates of 0.309 nm from HR-TEM is consistent with that of $BiVO_4$.[17] The surfaces of $BiVO_4$ plates are in turn decorated by $BiVO_4$ nanoparticles of ~2.5 nm diameter (QDs), uniformly dispersed at a density of ~ 3 QDs per 100 nm^2 (**Figure 1e,** inset). This morphology contrasts with that for bulk $BiVO_4$ wherein ~300-400 nm crystals were observed (**Figure S4**). Hydrothermal synthesis under mild conditions in the presence of PEG as a stabilizing agent therefore offers a simple means to generate $BiVO_4$ QDs, with ageing time and temperature likely critical to controlling particle size.[34]

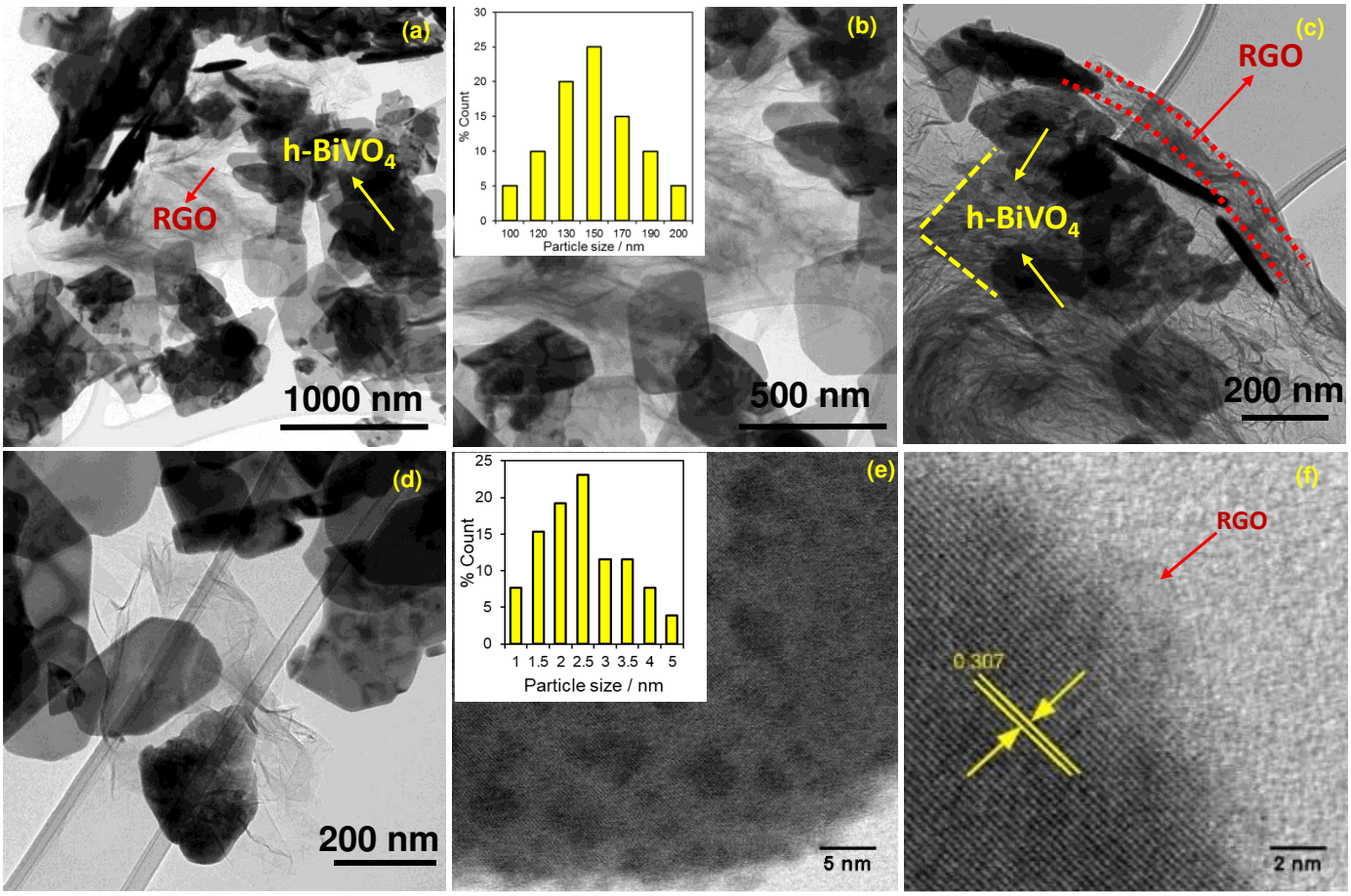

Figure 1. (a-f) HR-TEM images for h-$BiVO_4$/RGO. Inset to (b) shows particle size distribution of $BiVO_4$ plates and inset to (e) shows particle size distribution of h-$BiVO_4$.

Ethanolamine (MEA) is expected to act as both structure-directing agent favouring (010) $BiVO_4$ planes and a crosslinking agent promoting assembly of RGO into an aerogel-like assembly.[35] Formation of $BiVO_4$ is proposed to proceed as follows: under acidic conditions Bi^{3+} ions (from the nitrate precursor) react with VO_4^{3-} ions to nucleate primary $BiVO_4$ nanoparticles, this process is likely regulated by electrostatic interactions between Bi ions and PEG and pH regulation by MEA.[36, 37] Although a detailed mechanism is unclear, carboxylate and hydroxyl functional groups on RGO sheets increase their hydrophilicity (and hence dispersion in water) and interaction with PEG and ethanolamine may improve mixing with the h-$BiVO_4$ component in the final composite.

Crystallinity and the phase purity of the synthesized $BiVO_4$, h-$BiVO_4$ and h-$BiVO_4$/RGO were determined by XRD (**Figure 2a**). Reflections at 2θ = 18.67°, 28.96°, 30.54°, 34.51°, 39.78°, 42.49°, 46.64° and 52.23° are indexed to the (101), (112), (004), (200), (211), (015), (204) and (116) planes of monoclinic $BiVO_4$ with a scheelite structure (JCPDS No #14-0688), with parameters a = 5.19 Å; b = 5.08 Å, c = 11.69 Å and β =90.38. Additional weak reflections at 23.6° and 32.4° for h-$BiVO_4$ and h-$BiVO_4$/RGO are attributed to mixed phase tetragonal and monoclinic $BiVO_4$.[38, 39] Volume-averaged crystallite sizes **(Table 1)** estimated using the Scherrer equation suggest slightly smaller $BiVO_4$ crystallites (~26 nm) in the composite than the bulk $BiVO_4$ (~32 nm).

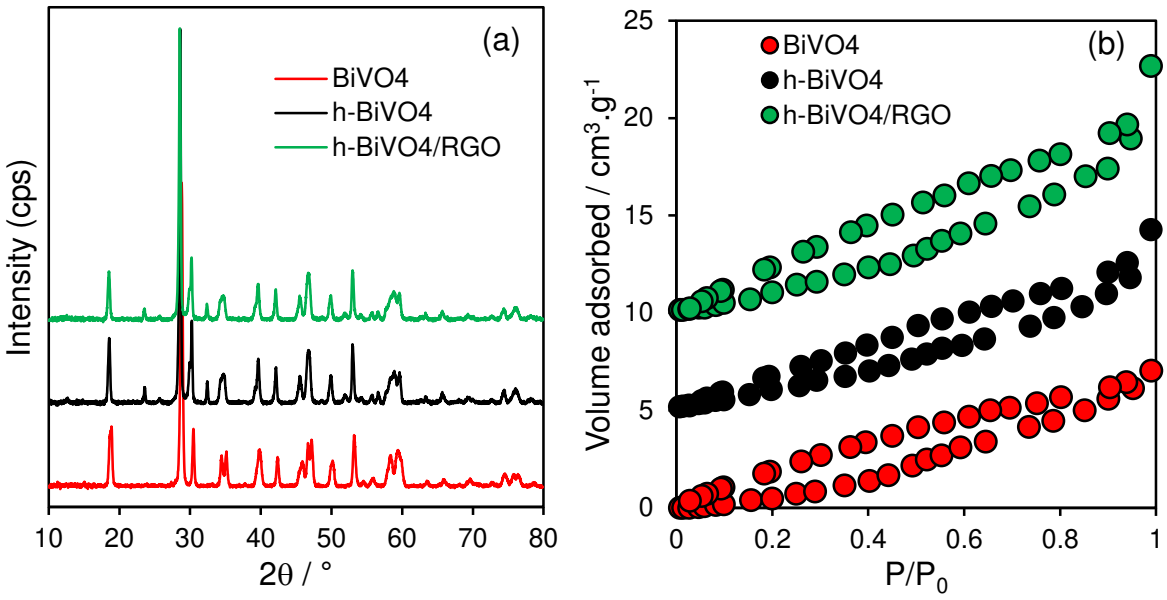

Figure 2. (a) XRD patterns, and (b) N_2 adsorption-desorption isotherms for $BiVO_4$, h-$BiVO_4$ and h-$BiVO_4$/RGO.

Table 1. Physicochemical properties of $BiVO_4$, h-$BiVO_4$ and h-$BiVO_4$/RGO.

Sample	Average $BiVO_4$ particle size[a] / nm		Crystallite size[b] / nm	BET surface area[c] / $m^2.g^{-1}$	Band gap[d] / eV	VB edge potential[d] / eV	CB edge potential[e] / eV
	Bulk	QDs					
$BiVO_4$	300–400	-	32.4	1.8	2.54	2.3	-0.21
h-$BiVO_4$	160–200	2–4	29.2	5.2	2.52	2.0	-0.52
h-$BiVO_4$/RGO	150	2–3	26.0	6.2	2.44	1.8	-0.66

[a]HR-TEM. [b]XRD from (112) reflection. [c]N_2 porosimetry. [d]DRUVS. [e]Valence band XPS and band gap.

Nitrogen adsorption-desorption isotherms (**Figure 2b**) and resulting BET analysis reveals similar surface areas for h-$BiVO_4$/RGO and h-$BiVO_4$ of 6 $m^2.g^{-1}$ and 5 $m^2.g^{-1}$ respectively, both significantly higher than that for bulk-like $BiVO_4$ of 2 $m^2.g^{-1}$. This is attributed to the high surface area-to-volume ratio of QDs and RGO sheets, which may also confer benefits by improving mass-transport and access to active sites..[17]

Diffuse reflectance UV-Vis spectroscopy (DRUVS) was subsequently used to study the optical properties of $BiVO_4$, h-$BiVO_4$ and h-$BiVO_4$/RGO (**Figure S5a**). All photocatalysts exhibited similar DRUV spectra, featuring strong absorption between 200-500 nm characteristic of monoclinic scheelite $BiVO_4$[40]. However, h-$BiVO_4$ and h-$BiVO_4$/RGO also exhibited a modest absorption extending from 500-800 nm, accounting for their yellow/yellowish green colours.[41, 42]

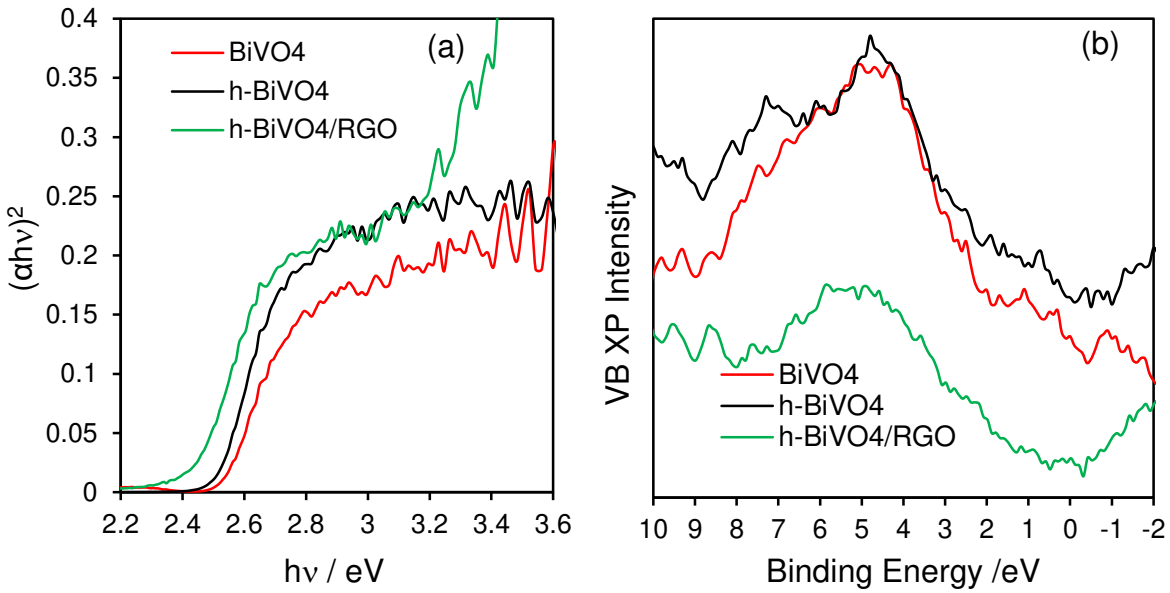

Figure 3. (a) Tauc plots derived from DRUVS spectra, and (b) valence band XP spectra of $BiVO_4$, h-$BiVO_4$ and h-$BiVO_4$/RGO.

The corresponding Tauc plots, presented in **Figure 3a** and **Figure S5b-d**, were calculated from **Eq. 4**:

$$\alpha h\nu = A(h\nu - E_g)^{\eta} \qquad \textbf{Eq. 4}$$

where α, h, ν, Eg and A are the absorption coefficient, Planck's constant, the frequency of light, the band gap energy and the proportionality constant, respectively. Band gaps were calculated using the Kubelka-Munk formula (**Eq. 5**):

$$a = \frac{(1-R)^2}{2R} \qquad \textbf{Eq. 5}$$

The resultant band gaps for the $BiVO_4$, h-$BiVO_4$ and h-$BiVO_4$/RGO spanned 2.54 to 2.44 eV (**Table 1**) being smallest for the nanocomposite; the bandgap for h-$BiVO_4$ was higher than reported values, likely due to the particle size effects and the presence of surface defects,[43] as previously reported for quantum-sized $BiVO_4$.[44] Recall that RGO only represents 2 wt% of the nanocomposite, and hence differences between the UV-Vis spectra of h-$BiVO_4$/RGO and h-$BiVO_4$ reflect modification of the vanadate electronic band structure. Valence band edge energies determined by XPS (**Figure 3b**) decreased from 2.3 eV, 2.0 eV and 1.8 eV for $BiVO_4$, h-$BiVO_4$ and h-$BiVO_4$/RGO respectively, all higher than the potential for water oxidation of 1.23 V NHE (at pH 0).[41]

Insight into charge carrier excitation and underlying e^--h^+ recombination processes was obtained through steady-state and time-resolved photoluminescence (PL) spectroscopy under 520 nm excitation (**Figure 4** and **Figure S6**). The resulting PL spectra evidenced lower intensity emissions for the h-$BiVO_4$ and h-$BiVO_4$/RGO photocatalysts than the bulk-like $BiVO_4$, and hence suppressed recombination for the former,[45] indicating charge separation at the interfaces between $BiVO_4$ plates and nanoparticles and/or RGO sheets.[46] Decay curves

of the corresponding time-resolved PL spectra could be adequately fitted using biexponential functions to derive photoexcited charge carrier lifetimes resulting from radiative and non-radiative processes as previously reported.[47, 48] Average decay lifetimes were similar for all photocatalysts, albeit slightly shorter (1.28 ns) for $BiVO_4$ than for h-$BiVO_4$ and h-$BiVO_4$/RGO (1.30 ns and 1.32 ns respectively) indicating relaxation from the same $BiVO_4$ states in all the materials.

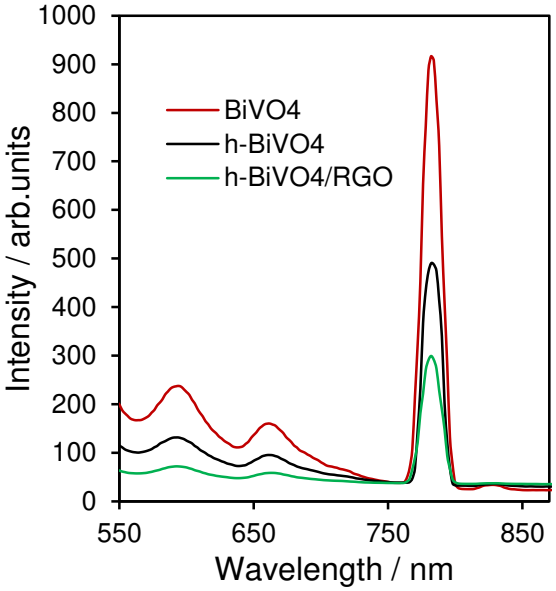

Figure 4. Photoluminescence steady-state excitation of $BiVO_4$, h-$BiVO_4$ and h-$BiVO_4$/RGO under 520 nm excitation at room temperature.

The surface composition and chemical environments in the photocatalysts were studied by high-resolution XPS (**Figure 5a-b**). Bi 4f XP spectra reveal two distinct chemical environments, with spin-orbit split $4f_{7/2}$ components at 157.6 eV and 159.1 eV binding energies, the latter is consistent with Bi^{3+} species in $BiVO_4$ and indeed dominates the spectra of our bulk-like $BiVO_4$ photocatalyst.[17, 49] The low binding energy species dominates the h-$BiVO_4$ and h-$BiVO_4$/RGO spectra and is attributed to Bi^{3+} species present in the vanadate nanoparticles. Note that quantum confinement effects typically increase the band gaps of groups II-VI semiconductors,[50] and for PbS are reported to shift Pd 4f core levels to higher binding energy,[51] opposite to the present observation. However, predicting such core level shifts requires a detailed analysis of the electronic band structure and quantification of surface defects which lies beyond this study. V 2p XP spectra also revealed two distinct chemical environments, with spin-orbit split V $2p_{3/2}$ components at 515.0 eV and 516.8 eV, respectively assigned to respective V^{4+} and V^{5+} surface species in $BiVO_4$.[49, 52] The high binding energy species again dominates the $BiVO_4$ spectra, consistent with V^{5+} in bulk-like VO_4^{3-} moieties within the large vanadate plates, whereas the low binding energy species dominates the h-$BiVO_4$ and h-$BiVO_4$/RGO spectra. Note that while the low binding energy species is attributed to surface V^{4+}, such assignments are hindered by the possible influence of surface defects and broad range of literature values for vanadium oxidation states. Successful incorporation of RGO was evidenced by C 1s XP spectra (**Figure S7**) with sp^2 C=C, C–O and C=O at 284.6 eV, 286.0 eV and 288.3 eV respectively.[53]

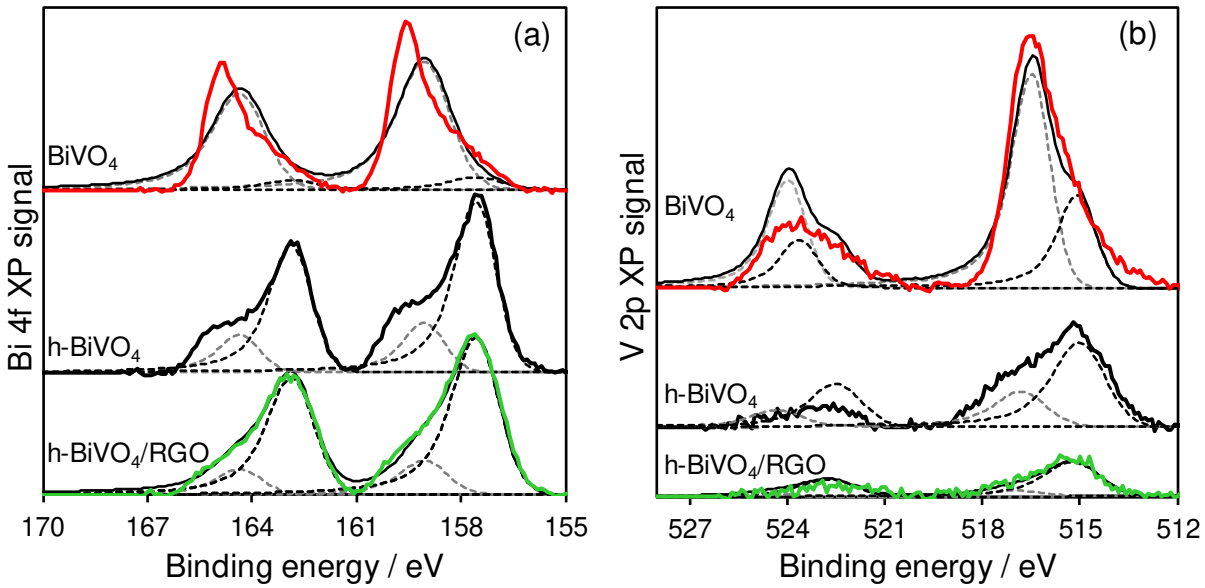

Figure 5. (a) Bi 4f and (b) V 2p XP spectra (spectra offset for clarity) for $BiVO_4$, h-$BiVO_4$ and h-$BiVO_4$/RGO.

Photocatalytic removal of bisphenol A

The photocatalytic degradation of (BPA under visible light irradiation was explored for h-$BiVO_4$/RGO, h-$BiVO_4$ and $BiVO_4$. Since BPA does not absorb visible light, such degradation studies are unaffected by artifacts arising from direct photochemical degradation which plague related studies of organic dye pollutants.[54] The concentrations of BPA and the major liquid phase photodegradation products, hydroquinone (HQ), benzoquinone (BQ) and maleic acid (MA), were determined by HPLC (**Figure S8a-c**), however evolved CO_2 was not measured in common with most reports. Mass normalized initial rates of BPA removal followed the order h-$BiVO_4$/RGO > h-$BiVO_4$ >> $BiVO_4$ (**Figure 6a**), with the h- $BiVO_4$ and h-$BiVO_4$/RGO respectively 3.5 and 4.5 times more active than $BiVO_4$. Normalizing for mass and surface area (**Figure 6b**) lowers these rate enhancements to ~1.3-1.4, suggesting that the higher surface area of the hierarchical $BiVO_4$ nanoplates/nanoparticles is largely responsible for their superior photocatalytic performance, with interfacial contact with RGO and/or improved visible light absorption (**Figure S5a**) conferring only minor advantages. After 120 min reaction, the extent of BPA removal was $BiVO_4$ (57 %) < h-$BiVO_4$ (65 %) < h-$BiVO_4$/RGO (72 %). These trends in photoactivity were mirrored by corresponding apparent quantum efficiencies (AQEs, see Supporting Information measured at 475 nm), which followed the order h-$BiVO_4$/RGO (15.1 %) > h-$BiVO_4$ (11.7 %) >> $BiVO_4$ (3.4 %) (**Figure S9**). There are no previous reports of AQE for BPA degradation over $BiVO_4$ photocatalysts. The performance of our h-$BiVO_4$/RGO > h-$BiVO_4$ photocatalysts compare favourably with that for CuO_x/$BiVO_4$ wherein 85 % BPA removal was reported,[55] despite photodegradation over the latter binary mixed semiconductor being aided by soluble bicarbonate radicals and a lower BPA concentration. In related work, Jiang et al. reported 96 % phenol removal over $BiVO_4$, however their system used additional H_2O_2 as a strong oxidant and a high intensity (300 W Xe lamp) light source.[56] The photocatalytic activity of our h-$BiVO_4$/RGO photocatalyst is benchmarked against literature systems for a range of organic molecules in **Table S1**. Comparisons are hindered by wide variations in catalyst loading,

reactant concentration, and light intensity, with no AQEs reported, however in general our h-$BiVO_4$/RGO exhibited the second highest rate of molecular degradation for the lowest catalyst loading under an intermediate light flux.

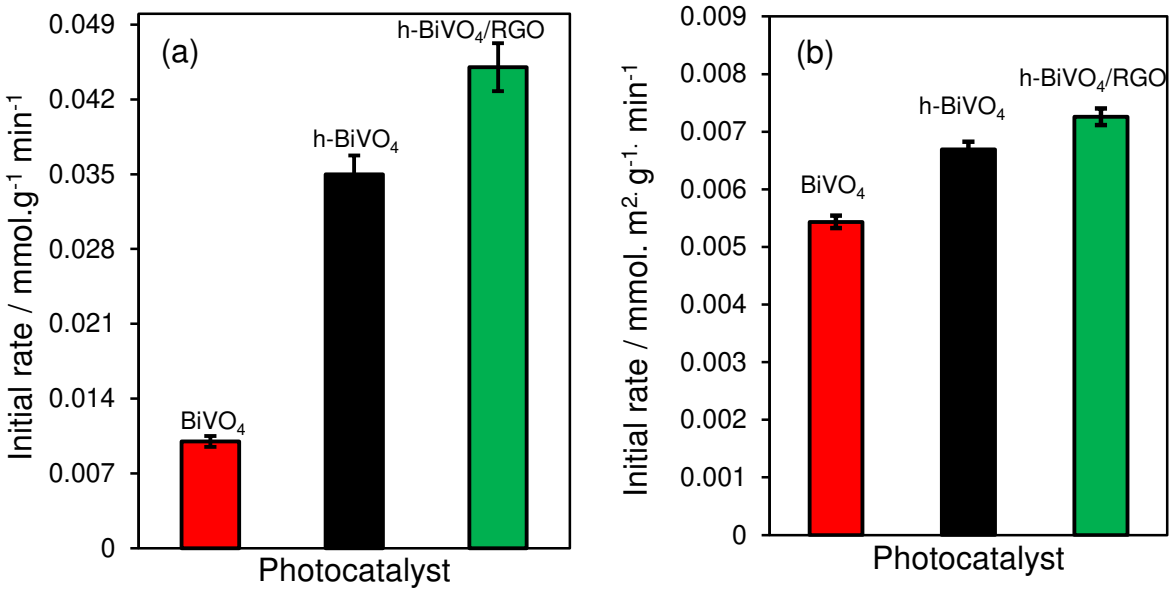

Figure 6. (a) Initial rates of BPA removal, and (b) surface area normalized initial rates of BPA removal over $BiVO_4$, h-$BiVO_4$ and h-$BiVO_4$/RGO. Experimental conditions: 50 mL BPA of 4.2 $\times 10^{-2}$ mM, 20 mg catalyst, 200 W Hg-Xe arc lamp with 420 nm visible cut-off filter.

The HQ, BQ and MA products of BPA photocatalytic degradation were monitored by HPLC as a function of reaction time to identify possible decomposition pathways (**Figure 7a-c**). Photocatalyst irradiation produces energetic holes which can react with water to form hydroxyl radicals ($^{\bullet}OH$) and photoexcited electrons able to react with oxygen to form superoxide radicals ($O_2^{-\bullet}$); the latter may further react with H_2O to yield $^{\bullet}OH$ radicals via redox reactions. For all three photocatalysts, HQ and BQ (in an approximately 2:1 molar ratio) were the minor photodegradation products, whose formation was coincident with that of the major MA product. The HQ and BQ concentrations peaked after 30 min photoirradiation, subsequently decaying to approximately two thirds of their maximum values and indicative of primary products, whereas the MA concentration increased monotonically with reaction time. The final MA yield increased from 35 % for $BiVO_4$ to 56 % for h-$BiVO_4$/RGO (**Figure 7d**), however the MA selectivity relative to all liquid products remained constant at 58 %, indicating a common active site and reaction mechanism for all threee photocatalysts.

Hydroxyl radical formation over the h-$BiVO_4$/RGO photocatalyst was confirmed by fluorescence spectroscopy. Briefly, an aqueous solution of terephthalic acid (TPA) was irradiated in the presence of h-$BiVO_4$/RGO and the subsequent emission spectra recorded as a function of irradiation time: in the presence of $^{\bullet}OH$ radicals TPA undergoes oxidation to 2-hydroxyterephthalic acid (HTPA), which is characterised by a 425 nm emission (**Figure S10**).

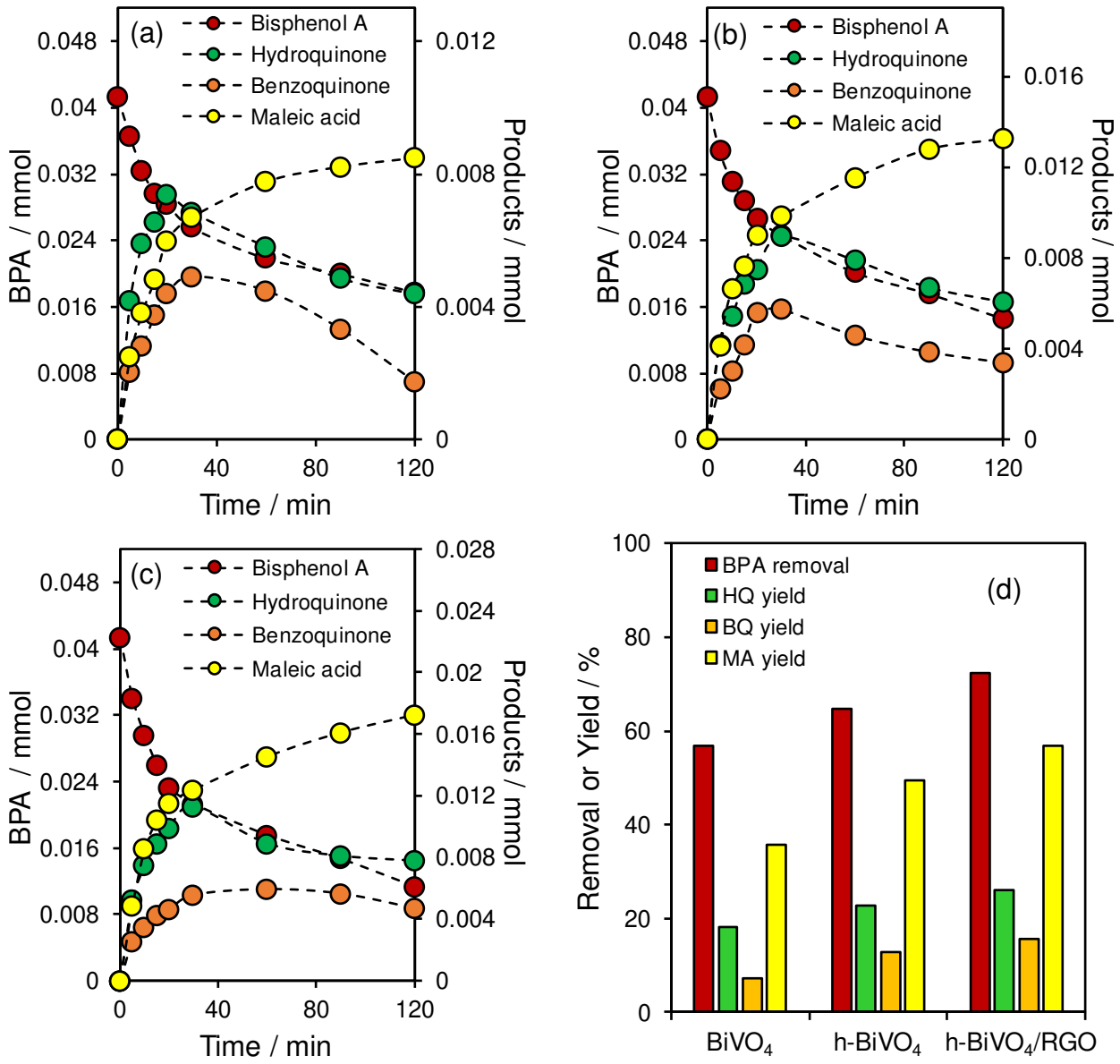

Figure 7. (a-c) Reaction profiles for photocatalytic BPA removal and resulting liquid phase product formation, and (d) comparative 2 h % BPA removal and product selectivity, over $BiVO_4$, h-$BiVO_4$ and h-$BiVO_4$/RGO. Note that decomposition of 1 mol of BPA yield 2 mols of MA. Experimental conditions: 50 mL BPA of 4.2 $\times 10^{-2}$ mM, 20 mg catalyst, 200 W Hg-Xe arc lamp with 420 nm visible cut-off filter.

The superior activity offered by the h-$BiVO_4$/RGO composite photocatalyst relative to h-$BiVO_4$ suggests the RGO acts as an acceptor and trap centre for electrons photoexcited at the semiconductor and transported across the interface,[57-59] consistent with the suppressed emission in **Figure 4**. Consequently, the following pathways for BPA photocatalytic degradation over h-$BiVO_4$/RGO are proposed in **Scheme 1**, based on observation of the preceding reaction products and the significance of in-situ photogenerated hydroxyl radicals

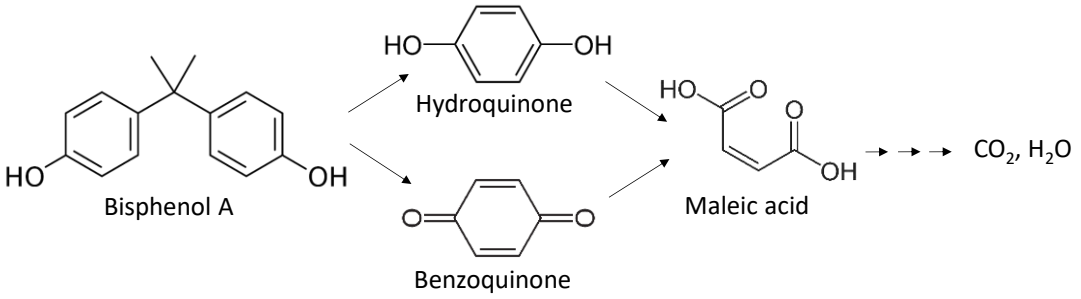

Scheme 1. Proposed reaction pathway for the photocatalytic oxidative degradation of BPA. Note complete mineralisation was not determined in this work.

Photocatalyst stability is a critical requirement for practical applications, and hence was investigated for the most active h-$BiVO_4$/RGO photocatalyst. Negligible deactivation was observed over five consecutive cycles of BPA photodegradation under visible light irradiation (**Figure S12**) consistent with excellent stability of crystalline monoclinic $BiVO_4$ by XRD (**Figure S13**) even after 10 h continuous photocatalysis.

Photocatalytic production of hydrogen

Vanadate photocatalysts were also examined for visible light H_2 production (**Figure 8a-b**) from water in the presence of ethanol as a hole scavenger. Resulting mass normalized initial rates following the order h-$BiVO_4$/RGO (11.5 $\mu mol.g^{-1}.h^{-1}$) > h-$BiVO_4$ (7.4 $\mu mol.g^{-1}.h^{-1}$) >> $BiVO_4$ (0.03 $\mu mol.g^{-1}.h^{-1}$), with corresponding AQEs of <0.01 %, 0.21% and 0.32% respectively (**Figure S11**). This order of photocatalyst reactivity also mirrors that of the corresponding conduction band minima calculated from valence band maxima and band gaps (**Table 1** and **Scheme 2**), and hence follow the reducing ability of photoexcited electrons responsible for proton reduction.[60] Hydrogen production rates for h-$BiVO_4$/RGO and h-$BiVO_4$ compare favourably with those reported under solar light for 50 nm $BiVO_4$ (2.78 $\mu mol.g^{-1}.h^{-1}$) with methanol as a sacrificial electron scavenger,[16] and 5 nm carbon quantum dot/$BiVO_4$ QD composites for overall water splitting (11.6 $\mu mol.g^{-1}.h^{-1}$).[17] The highest reported rate of H_2 evolution over $BiVO_4$ nanocrystals (10-20 nm) is 195.6 $mmol.h^{-1}$, however this was obtained under UV irradiation (240 W Hg-Xe lamp) with ethanol as a sacrificial reagent.[60] Photoelectrochemical H_2 evolution was also reported over a $BiVO_4$-RGO photoanode under visible light, with a productivity of 0.75 $\mu mol.h^{-1}$ obtained using a 0.8 V external bias,[24] although the photocatalyst loading was not reported. Enhanced photoactivity of our h-$BiVO_4$/RGO photocatalyst relative to bulk-like $BiVO_4$ is attributed to its higher surface area, extended visible light absorption, and more energetic photoexcited electrons (higher conduction band minimum); interfacial charge transfer in the nanocomposite may also account for its enhanced H_2 production relative to h-$BiVO_4$.

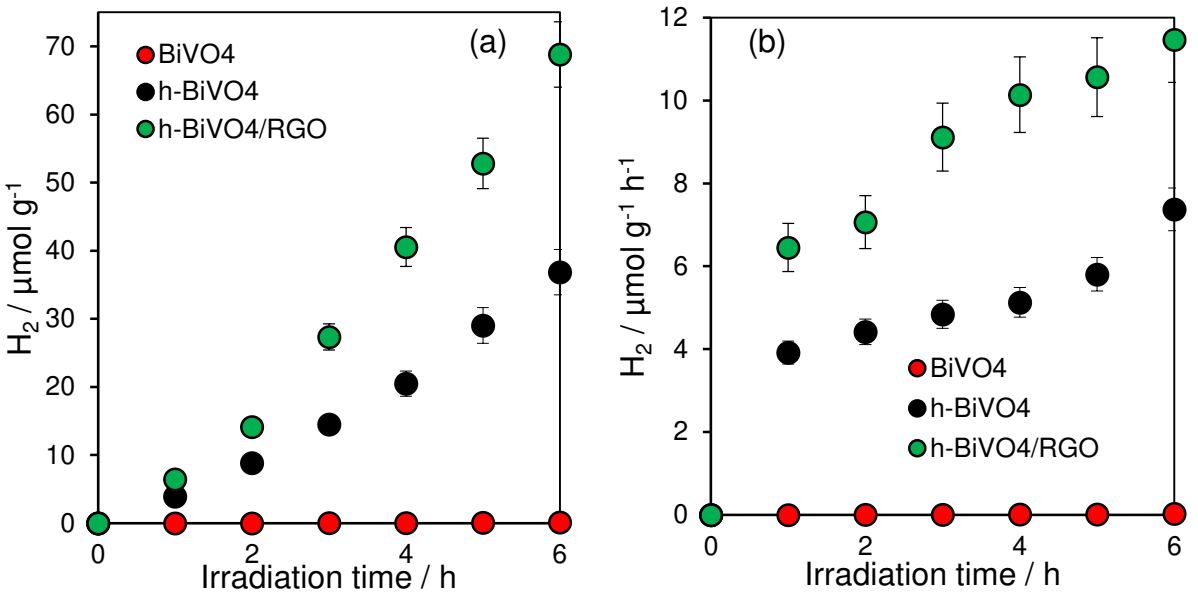

Figure 8. (a) Mass normalised hydrogen production, and (b) mass normalised rate of hydrogen production under visible light over $BiVO_4$, h-$BiVO_4$ and h-$BiVO_4$/RGO. Experimental conditions: 50 mg catalyst, 50 mL deionised water, 0.5 mL ethanol as a hole scavenger, 200 W Hg-Xe arc lamp with 420 nm visible cut-off filter.

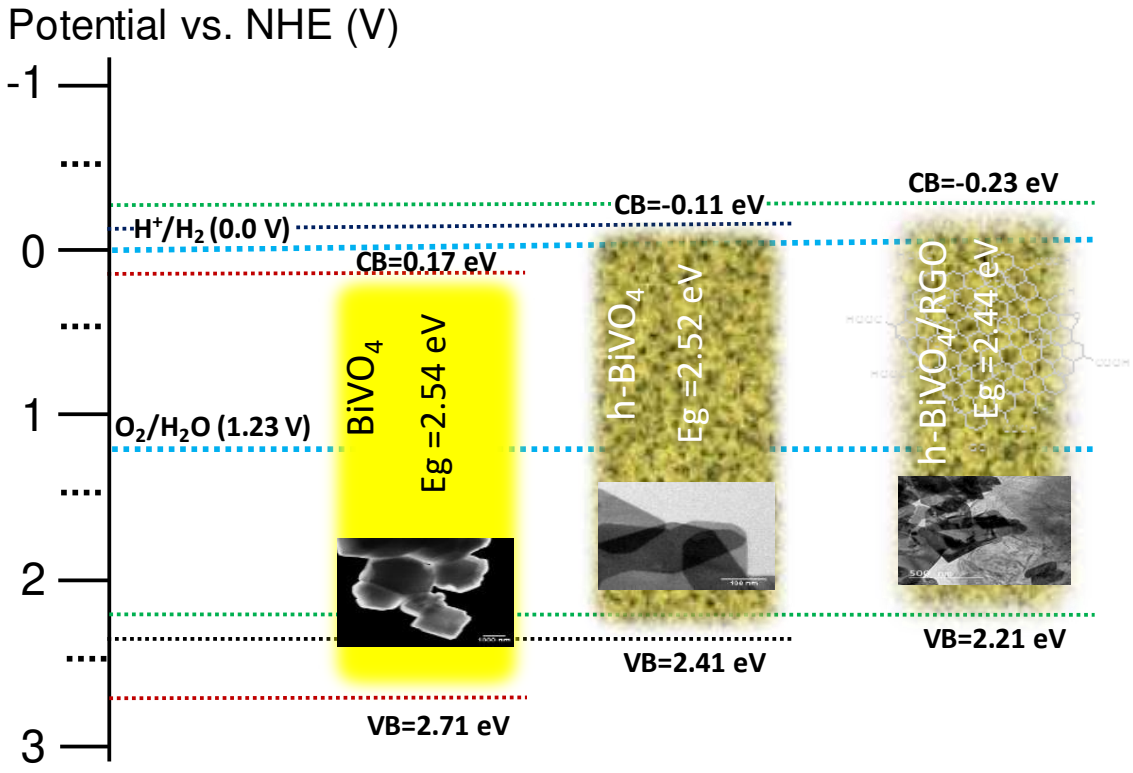

Scheme 2 Schematic of band edges for $BiVO_4$, h-$BiVO_4$ and h-$BiVO_4$/RGO, values from **Table 1** adjusted to pH 7.

Photoelectrochemical properties

The origin of the enhanced h-$BiVO_4$/RGO photoactivity was further investigated by transient photocurrent measurement, using chopped-light illumination (**Figure 9a**). Fast and reproducible photoresponses were obtained for all three vanadate photocatalysts, with photocurrent intensities following the order h-$BiVO_4$/RGO

> h-$BiVO_4$ >> $BiVO_4$. The approximately four-fold photocurrent enhancement for h-$BiVO_4$/RGO relative to $BiVO_4$ and literature reports[17] mirrors their relative activities for BPA degradation, and is again consistent with the higher surface area and greater visible light absorption of the nanocomposite. The more modest increase in photocurrent for h-$BiVO_4$/RGO versus h-$BiVO_4$ suggests that RGO sheets confer only a minor enhancement in the photoresponse,[61] attributed to improved separation of photogenerated charge carriers.

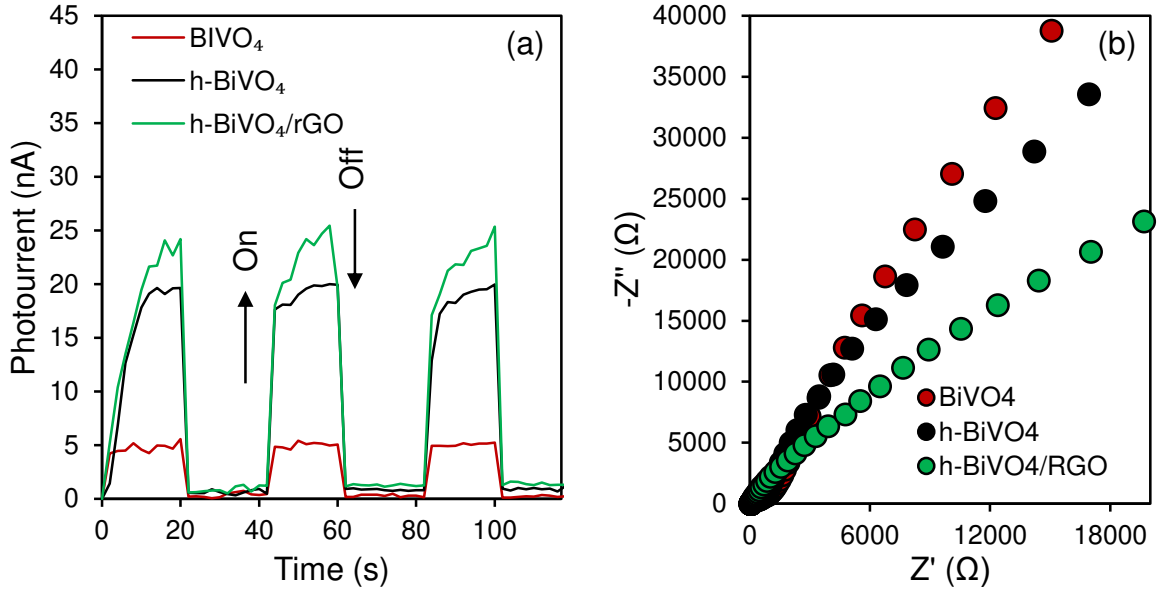

Figure 9. (a) Transient photocurrent signals, and (b) electrochemical impedance spectroscopy for $BiVO_4$, h-$BiVO_4$ and h-$BiVO_4$/RGO under visible light illumination (λ>420nm) using a 200 W Hg-Xe arc lamp and 0.5 M Na_2SO_4 electrolyte.

Charge transport behaviour was also studied by electrochemical impedance spectroscopy (**Figure 9b**). The radius of the impedance semicircle in the resulting Nyquist plots is inversely proportional to the rate of interfacial charge transfer in our photocatalysts.[62-65] The smallest was observed for h-$BiVO_4$/RGO, followed by h-$BiVO_4$ and then $BiVO_4$, indicating lower charge transfer resistance for the nanocomposite. This presumably reflects rapid electron transfer from the space charge region to the semiconductor-electrolyte surface mediated by the RGO nanosheets,[66] which is expected to suppress photoexcited charge carrier recombination.[67-69]

Conclusions

The one-pot hydrothermal synthesis of hierarchical $BiVO_4$ and $BiVO_4$/RGO nanocomposite photocatalysts using ethanolamine and polyethylene glycol as structure-directing agents is reported. Hierarchical (h-)$BiVO_4$ structures comprise ~150-200 nm plates decorated by ~2-4 nm nanoparticles with surface areas ~3-4 times greater than that of 300-400 nm $BiVO_4$ plates in the absence of structure-directing agents. Visible light absorption is also enhanced for h-$BiVO_4$/RGO and h-$BiVO_4$ photocatalysts associated with band gap narrowing, and accompanied by a change in the surface chemical environment of both Bi and V cations. Oxidative photocatalytic degradation of bisphenol-A (BPA) was observed under visible light irradiation,

driven by photogenerated hydroxyl radicals, with h-$BiVO_4$/RGO and h-$BiVO_4$ outperforming bulk-like $BiVO_4$. Hydroquinone and benzoquinone were minor (primary) products, alongside maleic acid as the major (secondary) product of BPA photodegradation, consistent with stepwise C-C bond cleavage and oxidation. The visible light photoactivity of h-$BiVO_4$/RGO for both BPA degradation and hydrogen production from a water/ethanol mix compares favourably with literature reports for related $BiVO_4$ photocatalysts under solar (UV-Vis) irradiation. Improved photoactivity for the hierarchical photocatalysts likely reflects a combination of higher surface areas and enhanced charge separation across the $BiVO_4$/RGO interface evidenced by steady-state photoluminescence and photoelectrochemical studies. These findings offer valuable insight into the design and fabrication of nanocomposite photocatalysts for environmental remediation and clean energy applications.

Supporting Information

Figure S1 HR-TEM images of h-$BiVO_4$ and corresponding particle size distributions of $BiVO_4$ plates. **Figure S2** HR-TEM images of h-$BiVO_4$. **Figure S3** Field emission SEM images of h-$BiVO_4$ and h-$BiVO_4$/RGO. **Figure S4** HR-TEM images of $BiVO_4$ and corresponding particle size distributions, and field emission SEM images of $BiVO_4$. **Figure S5** DRUV absorption spectra and corresponding Tauc plots. **Figure S6** time-resolved PL spectra. **Figure S7** core-level C1s XPS spectra of h-$BiVO_4$/RGO. **Figure S8** HPLC chromatograms of reaction mixtures after visible light photocatalytic degradation of BPA. **Figure S9** Apparent quantum efficiency for visible light photocatalytic degradation of BPA. **Figure S10** Photoluminescence spectra of 2-HPTA arising from TPA oxidation. **Table S1** Comparison of photocatalytic degradation of organic pollutants over $BiVO_4$ photocatalysts. **Figure S11** apparent quantum efficiency for H_2 evolution. **Figure S12** recycle tests for photocatalytic BPA degradation. **Figure S13** powder XRD patterns before and after photocatalytic BPA degradation. Apparent quantum efficiency (AQE) calculation.

Acknowledgements

We thank the Royal Society and Science and Engineering Research Board for the award of a Royal Society-SERB "Newton International Fellowship" to S.K. We acknowledge funding from the Biotechnology and Biological Sciences Research Council (BBSRC; via grant BB/P022685/1) and the European Commission H2020 Marie S Curie Research and Innovation Staff Exchange (RISE) award (Grant No. 871998). S. K. and K. S. would like to thank the Japan Society for the Promotion of Science (JSPS) for providing a postdoctoral fellowship for foreign researchers (P18387) and the research grant (KAKENHI JP18F18387). HR(S)TEM performed at the Ultra-microscopy Research Centre (URC) at Kyushu University.

Conflict of Interest

The authors declare no conflict of interest.

References

1. J. Gong, C. Li and M. R. Wasielewski, *Chemical Society Reviews*, 2019, **48**, 1862-1864.
2. P. Zhang and X. W. Lou, *Advanced Materials*, 2019, **31**, 1900281.
3. M. R. Hoffmann, S. T. Martin, W. Choi and D. W. Bahnemann, *Chemical reviews*, 1995, **95**, 69-96.
4. S. J. Moniz, S. A. Shevlin, D. J. Martin, Z.-X. Guo and J. Tang, *Energy & Environmental Science*, 2015, **8**, 731-759.
5. G. Mamba and A. Mishra, *Applied Catalysis B: Environmental*, 2016, **198**, 347-377.
6. Q. Li, X. Li, S. Wageh, A. A. Al-Ghamdi and J. Yu, *Advanced Energy Materials*, 2015, **5**, 1500010.
7. Y. Zhang, Z.-R. Tang, X. Fu and Y.-J. Xu, *ACS nano*, 2011, **5**, 7426-7435.
8. M. M. Khin, A. S. Nair, V. J. Babu, R. Murugan and S. Ramakrishna, *Energy & Environmental Science*, 2012, **5**, 8075-8109.
9. R. Costi, A. E. Saunders, E. Elmalem, A. Salant and U. Banin, *Nano Letters*, 2008, **8**, 637-641.
10. J. A. Seabold and K.-S. Choi, *Journal of the American Chemical Society*, 2012, **134**, 2186-2192.
11. K. J. McDonald and K.-S. Choi, *Energy & Environmental Science*, 2012, **5**, 8553-8557.
12. J. Hou, C. Yang, Z. Wang, S. Jiao and H. Zhu, *Applied Catalysis B: Environmental*, 2013, **129**, 333-341.
13. L. Ge, F. Zuo, J. Liu, Q. Ma, C. Wang, D. Sun, L. Bartels and P. Feng, *The Journal of Physical Chemistry C*, 2012, **116**, 13708-13714.
14. W. Gao, M. Wang, C. Ran and L. Li, *Chemical Communications*, 2015, **51**, 1709-1712.
15. L. Yu, Y. Huang, G. Xiao and D. Li, *Journal of Materials Chemistry A*, 2013, **1**, 9637-9640.
16. S. Sun, W. Wang, D. Li, L. Zhang and D. Jiang, *ACS Catalysis*, 2014, **4**, 3498-3503.
17. X. Wu, J. Zhao, S. Guo, L. Wang, W. Shi, H. Huang, Y. Liu and Z. Kang, *Nanoscale*, 2016, **8**, 17314-17321.
18. J. Wang, C. Liu, S. Yang, X. Lin and W. Shi, *Journal of Physics and Chemistry of Solids*, 2020, **136**, 109164.
19. K. S. Novoselov, A. K. Geim, S. V. Morozov, D. Jiang, Y. Zhang, S. V. Dubonos, I. V. Grigorieva and A. A. Firsov, *Science*, 2004, **306**, 666-669.
20. H. K. Chae, D. Y. Siberio-Pérez, J. Kim, Y. Go, M. Eddaoudi, A. J. Matzger, M. O'Keeffe and O. M. Yaghi, *Nature*, 2004, **427**, 523.
21. D. Deng, K. S. Novoselov, Q. Fu, N. Zheng, Z. Tian and X. Bao, *Nature Nanotechnology*, 2016, **11**, 218.
22. F. Meng, J. Li, S. K. Cushing, M. Zhi and N. Wu, *Journal of the American Chemical Society*, 2013, **135**, 10286-10289.
23. Y. Hou, F. Zuo, A. Dagg and P. Feng, *Nano Letters*, 2012, **12**, 6464-6473.
24. Y. H. Ng, A. Iwase, A. Kudo and R. Amal, *The Journal of Physical Chemistry Letters*, 2010, **1**, 2607-2612.
25. Y. Meng-Yang, Z. Zhi-Hao, H. Zhuo-Feng, L. Le-Quan, J. Hui-Ming, S. Zhu-Rui and M. Tian-Yi, *Angewandte Chemie International Edition*, 2017, **56**, 8407-8411.
26. X. Quanjun, C. Bei and Y. Jiaguo, *Angewandte Chemie International Edition*, 2015, **54**, 11350-11366.
27. C. Wang, H. Zhang, F. Li and L. Zhu, *Environmental science & technology*, 2010, **44**, 6843-6848.
28. J.-M. Lee, M.-S. Kim and B.-W. Kim, *Water Research*, 2004, **38**, 3605-3613.
29. Q. Han, H. Wang, W. Dong, T. Liu, Y. Yin and H. Fan, *Chemical Engineering Journal*, 2015, **262**, 34-40.
30. C. Mu, Y. Zhang, W. Cui, Y. Liang and Y. Zhu, *Applied Catalysis B: Environmental*, 2017, **212**, 41-49.
31. E. García-Díaz, D. Zhang, Y. Li, R. Verduzco and P. J. J. Alvarez, *Water Research*, 2020, **183**, 116095.
32. W.-K. Jo, S. Kumar, M. A. Isaacs, A. F. Lee and S. Karthikeyan, *Applied Catalysis B: Environmental*, 2017, **201**, 159-168.
33. Y. Qiu, K. Yan, H. Deng and S. Yang, *Nano Letters*, 2012, **12**, 407-413.
34. M. Xie, Z. Zhang, W. Han, X. Cheng, X. Li and E. Xie, *Journal of Materials Chemistry A*, 2017, **5**, 10338-10346.
35. Y. Li, Z. Sun, S. Zhu, Y. Liao, Z. Chen and D. Zhang, *Carbon*, 2015, **94**, 599-606.
36. H. Li, K. Yu, X. Lei, B. Guo, H. Fu and Z. Zhu, *The Journal of Physical Chemistry C*, 2015, **119**, 22681-22689.
37. M. Kakihana, *Journal of Sol-Gel Science and Technology*, 1996, **6**, 7-55.
38. M. Ge, L. Liu, W. Chen and Z. Zhou, *CrystEngComm*, 2012, **14**, 1038-1044.
39. Y. Zhao, R. Li, L. Mu and C. Li, *Crystal Growth & Design*, 2017, **17**, 2923-2928.
40. X. Xu, Q. Zou, Y. Yuan, F. Ji, Z. Fan and B. Zhou, *Journal of Nanomaterials*, 2014, **2014**, 401697.
41. W. J. Jo, H. J. Kang, K.-J. Kong, Y. S. Lee, H. Park, Y. Lee, T. Buonassisi, K. K. Gleason and J. S. Lee, *Proceedings of the National Academy of Sciences*, 2015, **112**, 13774-13778.
42. J. Yu and A. Kudo, *Advanced Functional Materials*, 2006, **16**, 2163-2169.
43. T. K. Townsend, N. D. Browning and F. E. Osterloh, *ACS Nano*, 2012, **6**, 7420-7426.
44. J. Sun, X. Li, Q. Zhao, M. O. Tadé and S. Liu, *Journal of Materials Chemistry A*, 2015, **3**, 21655-21663.
45. A. Mukherji, B. Seger, G. Q. Lu and L. Wang, *ACS nano*, 2011, **5**, 3483-3492.
46. D. K. Padhi and K. Parida, *Journal of Materials Chemistry A*, 2014, **2**, 10300-10312.
47. S. Cao, Q. Huang, B. Zhu and J. Yu, *Journal of Power Sources*, 2017, **351**, 151-159.

48. M. Athanasiou, R. Smith, B. Liu and T. Wang, *Scientific reports*, 2014, **4**, 7250.
49. K. R. Tolod, S. Hernández, M. Castellino, F. A. Deorsola, E. Davarpanah and N. Russo, *International Journal of Hydrogen Energy*, 2020, **45**, 605-618.
50. A. L. E. and and M. Rosen, *Annual Review of Materials Science*, 2000, **30**, 475-521.
51. A. I. Kovalev, D. L. Wainstein, A. Y. Rashkovskiy, A. Osherov and Y. Golan, *Surface and Interface Analysis*, 2010, **42**, 850-854.
52. S. Poulston, N. J. Price, C. Weeks, M. D. Allen, P. Parlett, M. Steinberg and M. Bowker, *Journal of Catalysis*, 1998, **178**, 658-667.
53. M. R. Karim, H. Shinoda, M. Nakai, K. Hatakeyama, H. Kamihata, T. Matsui, T. Taniguchi, M. Koinuma, K. Kuroiwa and M. Kurmoo, *Advanced Functional Materials*, 2013, **23**, 323-332.
54. N. Barbero and D. Vione, *Environmental Science & Technology*, 2016, **50**, 2130-2131.
55. Y. Kanigaridou, A. Petala, Z. Frontistis, M. Antonopoulou, M. Solakidou, I. Konstantinou, Y. Deligiannakis, D. Mantzavinos and D. I. Kondarides, *Chemical Engineering Journal*, 2017, **318**, 39-49.
56. H. Jiang, H. Dai, X. Meng, K. Ji, L. Zhang and J. Deng, *Applied Catalysis B: Environmental*, 2011, **105**, 326-334.
57. S. Yuanhua, Z. Zhenhuan, T. Jian, H. Pin, J. Huaidong, L. Hong and C. J. P., *Small*, 2014, **10**, 3775-3782.
58. A. Hagfeldt and M. Graetzel, *Chemical Reviews*, 1995, **95**, 49-68.
59. H. Wang, L. Zhang, Z. Chen, J. Hu, S. Li, Z. Wang, J. Liu and X. Wang, *Chemical Society Reviews*, 2014, **43**, 5234-5244.
60. G. Nagabhushana, G. Nagaraju and G. Chandrappa, *Journal of Materials Chemistry A*, 2013, **1**, 388-394.
61. F. Ning, M. Shao, S. Xu, Y. Fu, R. Zhang, M. Wei, D. G. Evans and X. Duan, *Energy & Environmental Science*, 2016, **9**, 2633-2643.
62. A. Xiaoqiang, L. Kimfung and T. Junwang, *ChemSusChem*, 2014, **7**, 1086-1093.
63. W. Shi, H. Ren, M. Li, K. Shu, Y. Xu, C. Yan and Y. Tang, *Chemical Engineering Journal*, 2020, **382**, 122876.
64. W. Shi, C. Liu, M. Li, X. Lin, F. Guo and J. Shi, *Journal of Hazardous Materials*, 2020, **389**, 121907.
65. F. Guo, M. Li, H. Ren, X. Huang, K. Shu, W. Shi and C. Lu, *Separation and Purification Technology*, 2019, **228**, 115770.
66. X. Wan, F. Niu, J. Su and L. Guo, *Physical Chemistry Chemical Physics*, 2016, **18**, 31803-31810.
67. F. Su, T. Wang, R. Lv, J. Zhang, P. Zhang, J. Lu and J. Gong, *Nanoscale*, 2013, **5**, 9001-9009.
68. Y. Wang, W. Wang, H. Mao, Y. Lu, J. Lu, J. Huang, Z. Ye and B. Lu, *ACS Applied Materials & Interfaces*, 2014, **6**, 12698-12706.
69. T. Wang, C. Li, J. Ji, Y. Wei, P. Zhang, S. Wang, X. Fan and J. Gong, *ACS Sustainable Chemistry & Engineering*, 2014, **2**, 2253-2258.